Case Studies in Construction Materials 19 (2023) e02410

Contents lists available at ScienceDirect

Case Studies in Construction Materials

journal homepage: www.elsevier.com/locate/cscm

Ternary cementless composite based on red mud, ultra-fine fly ash, and GGBS: Synergistic utilization and geopolymerization mechanism

Zhiping Li[a], Mengshi Gao[a], Zuxiang Lei[a,*], Lihong Tong[a], Junbo Sun[b], Yufei Wang[c], Xiangyu Wang[a], Xi Jiang[d,*]

[a] *School of Civil Engineering and Architecture, East China Jiaotong University, Nanchang 330013, China*
[b] *Institute for Smart City of Chongqing University In Liyang, Chongqing University, Jiangsu 213300, China*
[c] *School of Design and Built Environment, Curtin University, Perth, WA 6102, Australia*
[d] *Department of Civil and Environmental Engineering, The Hong Kong Polytechnic University, Hung Hom, Kowloon, Hong Kong Special Administrative Region*

ARTICLE INFO

Keywords:
Solid waste utilisation
Ternary geopolymer
Sustainability
Microstructure analysis
Red mud

ABSTRACT

Industrial solid wastes, such as ultra-fine fly ash (RUFA) and ground granulated blast-furnace slag (GGBS), hold tremendous potential for recycling due to their abundance and excellent pozzolanic properties. However, red mud (RM), a highly alkaline waste, has not received comprehensive attention in the construction industry. Thus, this study investigates the synergistic effect and geopolymerization mechanism of industrial solid wastes in ternary cementless composites based on RM, RUFA, and GGBS. The experimental program includes macroscopic comparative analyses of water consumption, fluidity, setting time, permeability, and compressive strength of the ternary cementless composite. Additionally, SEM and EDS analyses examine the microscopic morphology and elemental distribution of the composite. The results indicate that RM prolongs the setting time while reducing fluidity and compressive strength. A 30% increase in RM content led to a substantial rise in the initial and final setting time by approximately 191.6% and 164.7%, respectively. In contrast, GGBS enhances the compressive characteristics of the composite systems but shortens the setting time and reduces fluidity. Notably, Group D4 demonstrates the highest compressive strength, reaching an impressive 47.3 MPa. Moreover, the content of GGBS influences the hydration products in the ternary cementless composite. At low GGBS content, the material contains a significant amount of N-A-S-H gels, whereas at high GGBS content, partial N-A-S-H gels are replaced by C-A-S-H gels. These findings significantly enhance our understanding of the synergistic effect and geopolymerization mechanism of RM, RUFA, and GGBS, thereby facilitating the reuse of these three industrial solid wastes.

1. Introduction

The discharge of a significant volume of solid waste from industrial production has resulted in severe ecological destruction and environmental pollution, particularly in terms of water and soil contamination. As a result, there is a growing focus on the efficient

---

* Corresponding authors.
E-mail addresses: zxlei@ecjtu.edu.cn (Z. Lei), xijiang@polyu.edu.hk (X. Jiang).

https://doi.org/10.1016/j.cscm.2023.e02410
Received 20 June 2023; Received in revised form 1 August 2023; Accepted 16 August 2023

utilization and safe disposal of solid waste. For instance, fly ash (FA) has been extensively studied due to its diverse pozzolanic properties [1–3]. These solid wastes are increasingly being employed as supplementary cementitious materials (SCMs) in concrete, owing to their technical, economic, and environmental benefits. The incorporation of various industrial wastes either as a blend with clinker to produce cement or as separate ingredients in concrete is driven by economic considerations as well as the desire to enhance the durability and long-term strength of concrete structures.

Red mud (RM) is a highly alkaline waste generated from bauxite alumina production [4–9]. Due to its complex mineral composition, fine particle size, and high alkalinity, RM poses challenges for recycling [10]. Currently, only a small fraction, ranging from 4% to 5.2% of RM is recycled and reused [11,12]. Consequently, there has been a continuous accumulation of RM reserves. A significant amount of RM is often stored in dumpsite stockpile dams [13–17], occupying valuable land and potentially leading to groundwater pollution [18–22]. Furthermore, the fine particles of RM can contribute to air pollution when dispersed by wind [23]. Despite these challenges, RM, primarily composed of Al_2O_3, SiO_2 and Fe_2O_3 [24], holds substantial potential for utilization in geopolymers. Researchers have explored the properties of RM and its incorporation as an aluminosilicate precursor in geopolymer applications. For example, Zhang et al. [25] investigated geopolymer slurries incorporating blast furnace slag and RM, observing a decrease in fluidity with increasing RM particle size. Wang et al. [26] examined the mechanical properties, chemical compositions, and microstructure characterization of Bayer RM and Sintering RM using XRD, TG, and SEM analyses. They also conducted tests on strength, particle size, density, and hydraulic properties of RM. Significant differences were observed in the fundamental chemical composition between sintered RM and Bayer RM. Bayer RM exhibited finer and more dispersed microparticles, whereas Sintering RM exhibited higher shear strength. Hu et al. [27] developed geopolymers as construction materials using RM and three types of fly ash (FA), highlighting the beneficial influence of RM's high alkalinity on geopolymerization.

Fly ash (FA) is a residual waste produced by coal-fired power plants and is commonly used in the geopolymer industry. However, its widespread application is limited due to quality issues that prevent it from meeting requirements. To improve the reactivity of FA and meet quality standards, chemical or physical processes are often employed as pre-treatment methods [28,29]. One commonly used pre-treatment process is mechanical grinding, which activates FA and produces a finer version known as ultra-fine fly ash (RUFA) [30,31]. RUFA has smaller particle size and larger specific surface area compared to FA, with approximately double the specific surface area. Additionally, RUFA exhibits higher reactivity due to its finer grains. Several researchers have successfully utilized RUFA, a new industrial by-product, in the preparation of cementitious materials [32]. The high pozzolanic activity and amorphous structure of RUFA contribute to the development of geopolymer composites with impressive mechanical strength, reaching up to 97.6 MPa when activated by NaOH solution [33].

The utilization of FA in the synthesis of geopolymers has been extensively explored in various research studies. Furthermore, the combination of RM and FA has shown potential in producing geopolymer products with enhanced properties. Yang et al. [34] conducted a study where geopolymers were prepared using RM slurry and FA powder, and it was observed that the strength of these geopolymers remained stable at temperatures up to 600 °C. However, the mechanical properties, such as Young's modulus and compressive strength, exhibited a rapid decline beyond 600 °C. In another study by Choo et al. [35], FA was employed as an aluminosilicate precursor and RM served as an alkaline activator for synthesizing geopolymers based on FA. Their research demonstrated the successful synthesis of alkali-activated FA using RM as the activator. Ternary geopolymer composites have also been investigated in several studies, highlighting the synergistic effects of combining industrial solid wastes [36–43]. Chen et al. [44] developed ternary geopolymer composites using RM, reactive RUFA, and recycled powder activated by sodium silicate and NaOH. They systematically studied the macroscopic properties and microscopic characteristics of these composites, achieving impressive compressive strength of up to 46 MPa. Besides, P et al. [45] studied the influence of different proportions of the powder waste glass on the workability, mechanical and microstructural characterizations of composite with blast furnace slag, metakaolin and waste glass powder. The results of the experiments showed that the optimum percentage of replacement of the waste glass powder is 35% [46–48]. Taye et al. [49] developed a novel geopolymer utilizing RM, FA, and hemp fibers. They demonstrated that the addition of hemp fibers increased the strength of the geopolymer and altered the damage mechanism of the geosynthetics.

However, despite the potential benefits, there remains a notable research gap concerning a comprehensive understanding of the synergistic effects and geopolymerization mechanism in blended composites involving RM, RUFA, and GGBS. To address this knowledge gap and shed light on the synergistic effect and geopolymerization mechanism of industrial solid wastes, we have undertaken a study involving a ternary cementless composite consisting of RUFA, RM, and GGBS, with the intention of on-site application. Sodium silicate and hydroxide solution (NaOH) were used as alkaline activators in combination with the industrial solid wastes. The properties of the composite, such as the water consumption at standard consistency, fluidity, setting time, and mechanical properties, were comprehensively analyzed to determine the optimal formulation. Additionally, the mineral composition and microstructure of representative samples were characterized using SEM/EDS analysis. The main objective of this study is to foster the reuse of these three industrial by-products and offer valuable insights into augmenting traditional cement applications. The findings from our research hold important implications for sustainable waste management practices and the advancement of alternative cementitious materials.

2. Materials and methods

2.1. Raw materials

The selected raw materials for geopolymer synthesis contain RUFA, RM, and GGBS. Prior to use, the RM was sieved through a 0.15 mm screen mesh, while RUFA and GGBS were used directly. The particle size distribution (PSD) of the material is shown in Fig. 1, and their chemical oxide composition obtained from X-ray fluorescence spectroscopy (XRF) is listed in Table 1. The RUFA, obtained from Henan Jinrun New Materials Co. Ltd., has a density of 2.45 g/cm^3. The RM is sourced from Shandong Weiqiao Pioneering Group Co. Ltd. The GGBS, obtained from Longze Water Purification Materials Co. Ltd., has a density of 2.89 g/cm^3. The alkali activator used in the synthesis consists of sodium silicate solution (SSS) and NaOH. The SSS solution comprises 32 wt% silica, 14.34 wt% sodium oxide, and 53.66 wt% water. X-ray diffraction (XRD) analysis was conducted to examine the mineral composition of the materials. The RM predominantly contains hematite as the main crystalline phase, along with the presence of quartz and calcium aluminum oxides. Both RUFA and GGBS exhibit amorphous phases without distinct crystallization peaks. SEM analysis was performed on the raw materials, and the microstructure and SEM images of these three materials are illustrated in Fig. 2. The magnification of (1), (3), (5) is 2000 times, (4), (6) is 20,000 times and (2) is 10,000 times.

2.2. *Mixture proportions and sample preparation*

Table 2 displays the mixing proportions of all the samples used in the experiments. Experiment 1 aimed to study the impact of replacing RUFA with RM on the properties of composites based on RUFA. Experiments 2 and 3 were conducted to examine the effects of replacing RUFA with GGBS and replacing RM with GGBS, respectively, on the properties of RUFA/RM-based composites. Lastly, in experiment 4, the primary objective was to examine the impact of the solution/binder (S/B) ratio on the properties of the ternary composites. The experimental process is illustrated in Fig. 3. The content of NaOH in the mixture was 3.25 wt%, while the sodium silicate solution constituted 30 wt% of the mixture.

To make the specimens, it is necessary to prepare the alkali-activated solution and then mix the powder with the alkali-activated solution. To produce the alkali-activated solution, granular NaOH is combined with sodium silicate solution and water in a beaker, which is then thoroughly homogenized using a glass rod. Subsequently, the completed alkali-activated solution is left at room temperature for 24 h to allow it to cool before being used. Once the alkali-activated solution is ready, the RUFA/RM/GGBS cementless composite is prepared in a JJ-5 mixer. All solid materials are initially premixed for 60 s at low speed. Then, the FDN (a specific component) is dissolved in the finished alkali-activated solution. Next, the alkali-activated solution is added to the solid materials and mixed for 60 s at low speed. At last, the mixing process continues at high speed for 120 s. Subsequently, the fresh pastes are cast into molds. It is worth noting that the specimens demonstrate minimal drying shrinkage and do not display any surface cracks.

2.3. *Experimental methods*

2.3.1. *Fresh and hardened tests*

The water consumption at standard consistency of the composites was determined following the procedure outlined in the GB/T1346–2011 standard. The test involved measuring the amount of water required to achieve the standard consistency of the mixture. The standard consistency is reached when the test pin stops sinking and a distance of 6 ± 1 mm is maintained between the test rod and the base of the test mold. At this point, the quantity of water used is recorded as the standard consistency water consumption. The water demand test was tested three times and the average value was taken as the result.

The initial and final setting times of the composite slurry were determined using the Vicat apparatus and a conical model, following the guidelines outlined in GB/T 1346–2011. The conical model used for the test has a bottom inner diameter of 100 mm, an upper inner diameter of 70 mm, and a height of 60 mm. To determine the initial setting time, the alkali-activated solution was added to the composite slurry. The time at which the distance between the initial setting test needle and the bottom glass plate reached 4 mm ± 1 mm was recorded as the initial setting time. For the final setting time, a circular final setting test needle was used. The time at

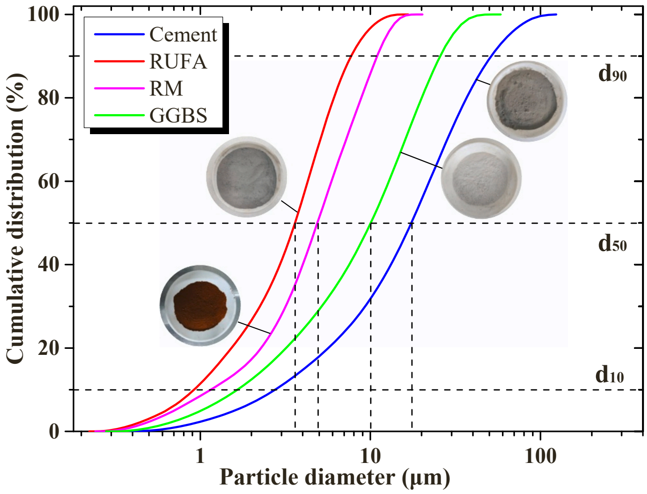

Fig. 1. The appearance and PSD of raw materials.

Table 1
Physical and chemical properties (wt%) of the raw materials.

	RUFA	RM	GGBS
Al_2O_3	25.67	25.11	13.7
SiO_2	58.7	16.93	31.1
CaO	4.74	6.02	40.9
Na_2O	1.94	11.6	0.38
Fe_2O_3	4.3	36.43	0.647
MgO	1.75	0.67	9.16
TiO_2	1.16	1.54	1.26
Others	1.74	1.7	2.853
Loss of ignition (%)	2.8	-	0.96
Density (g/cm^3)	2.55	3.46	2.93
Blaine surface area (cm^2/g)	44360	22300	4240

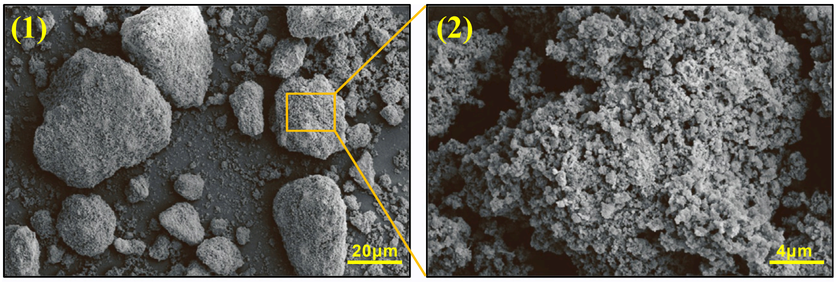

(a) Red mud

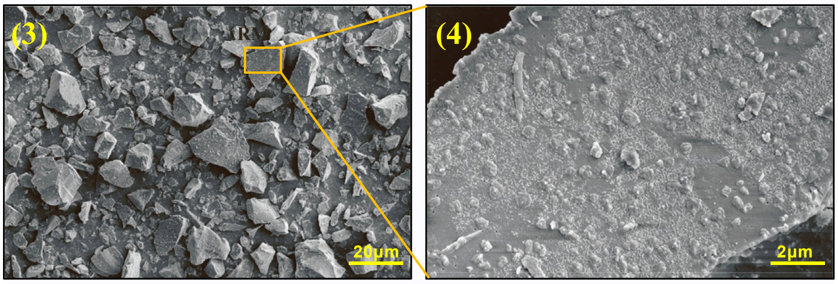

(b) Blast furnace slag

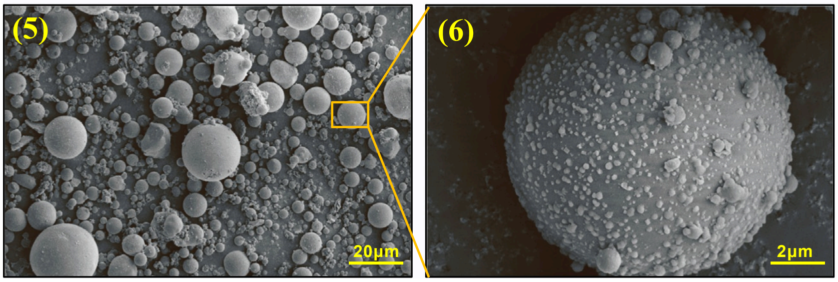

(c) Ultra-fine fly ash

Fig. 2. The microstructure and SEM analysis of raw materials.

which the final setting test needle did not leave any visible traces on the sample was recorded as the final setting time. In order to obtain more accurate results, the initial and final setting times were tested three times.

The fluidity tests were performed according to the specifications outlined in GB/T 8077–2012. In the fluidity test, a conical model was utilized. The model had a height of 60 mm, and its bottom and top internal diameters were 60 mm and 36 mm, respectively. To conduct the test, the slurry was poured into the conical model, which was placed on a wet glass plate. Subsequently, the model was lifted vertically, allowing the slurry to flow freely. After the slurry had flowed for a duration of 60 s, the maximum diameter in two vertical directions was measured using a ruler. The average value of these two measurements was then recorded as the fluidity of the slurry. The results of fluidity were calculated based on the average results of three samples.

The compressive strength tests were conducted in accordance with the specifications outlined in GB/T 17671–2021. The samples

Table 2
Mixture design and surface area of the samples.

Notation	RUFA (wt%)	RM (wt%)	GGBS (wt%)	PC (wt%)	NaOH (wt%)	SSS (wt%)	S/B	SSA (cm^2/g)	Remarks
B1	100				3.25	30	0.45	44,360	Experiment 1 (Binary group)
B2	90	10			3.25	30	0.45	42,154	
B3	80	20			3.25	30	0.45	39,948	
B4	70	30			3.25	30	0.45	37,742	
C1	70	20	10		3.25	30	0.45	35,936	Experiment 2 (Ternary group)
C2	60	20	20		3.25	30	0.45	31,924	
C3	50	20	30		3.25	30	0.45	27,912	
C4	40	20	40		3.25	30	0.45	23,900	
D1	50	40	10		3.25	30	0.45	31,524	Experiment 3 (Ternary group)
D2	50	30	20		3.25	30	0.45	29,718	
D3	50	20	30		3.25	30	0.45	27,912	
D4	50	10	40		3.25	30	0.45	26,106	
E1	60	20	20		3.25	30	0.4	31,924	Experiment 4 (Ternary group)
E2	60	20	20		3.25	30	0.45	31,924	
E3	60	20	20		3.25	30	0.5	31,924	
E4	60	20	20		3.25	30	0.55	31,924	
A0				100			0.45	3400	Experiment 5 (Control group)

S/B: Solution-to-binder ratio
SSA: Specific surface area

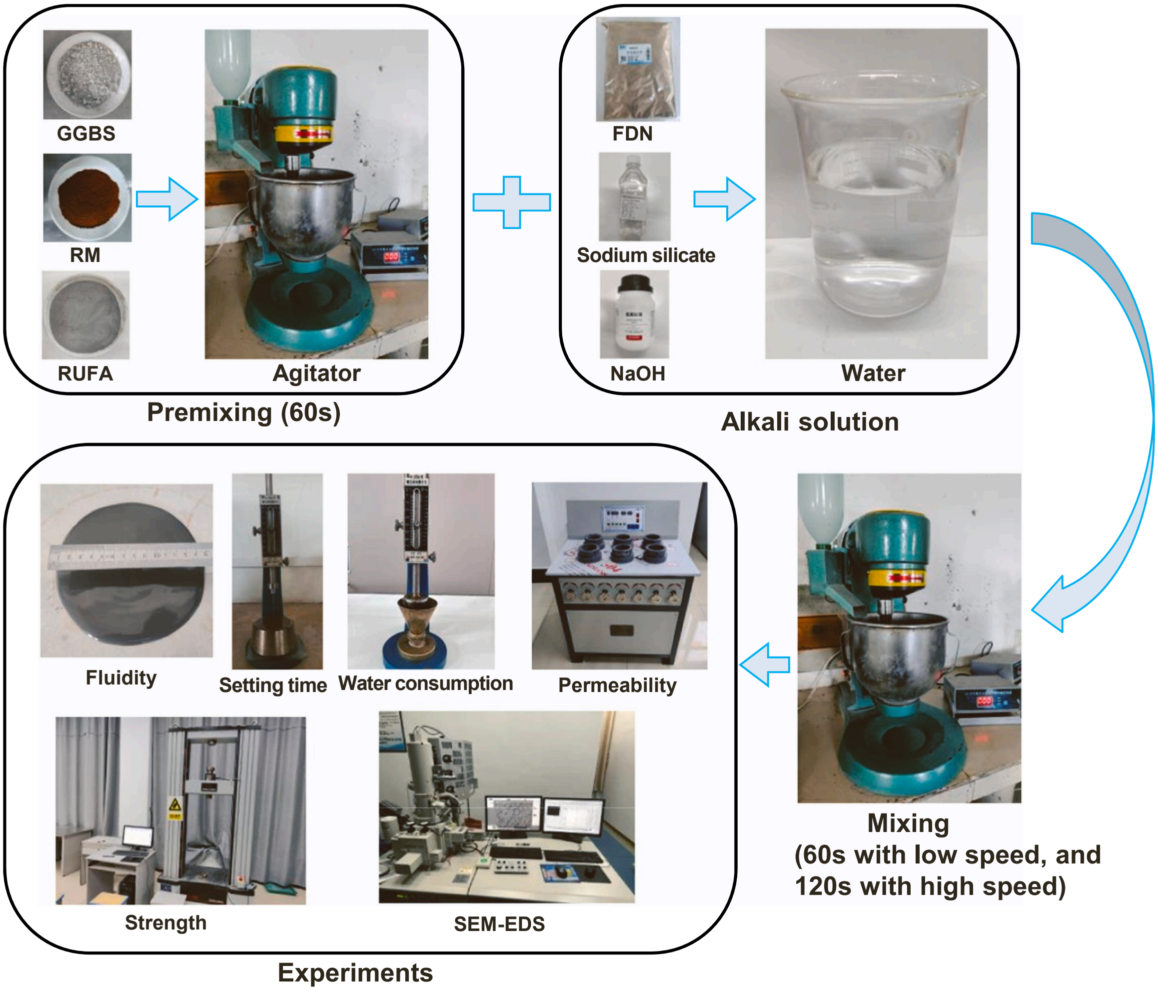

Fig. 3. Mixing procedures and test items of the samples.

were cured in a standard curing box maintained at a temperature of 20 ℃ and a relative humidity of 95%. After 24 h of curing, the samples were demoulded and then placed back into the curing box for further curing. In this study, the compressive strength tests were carried out at three different time periods: 1 day, 3 days, and 28 days. These time intervals allow for the assessment of the compressive

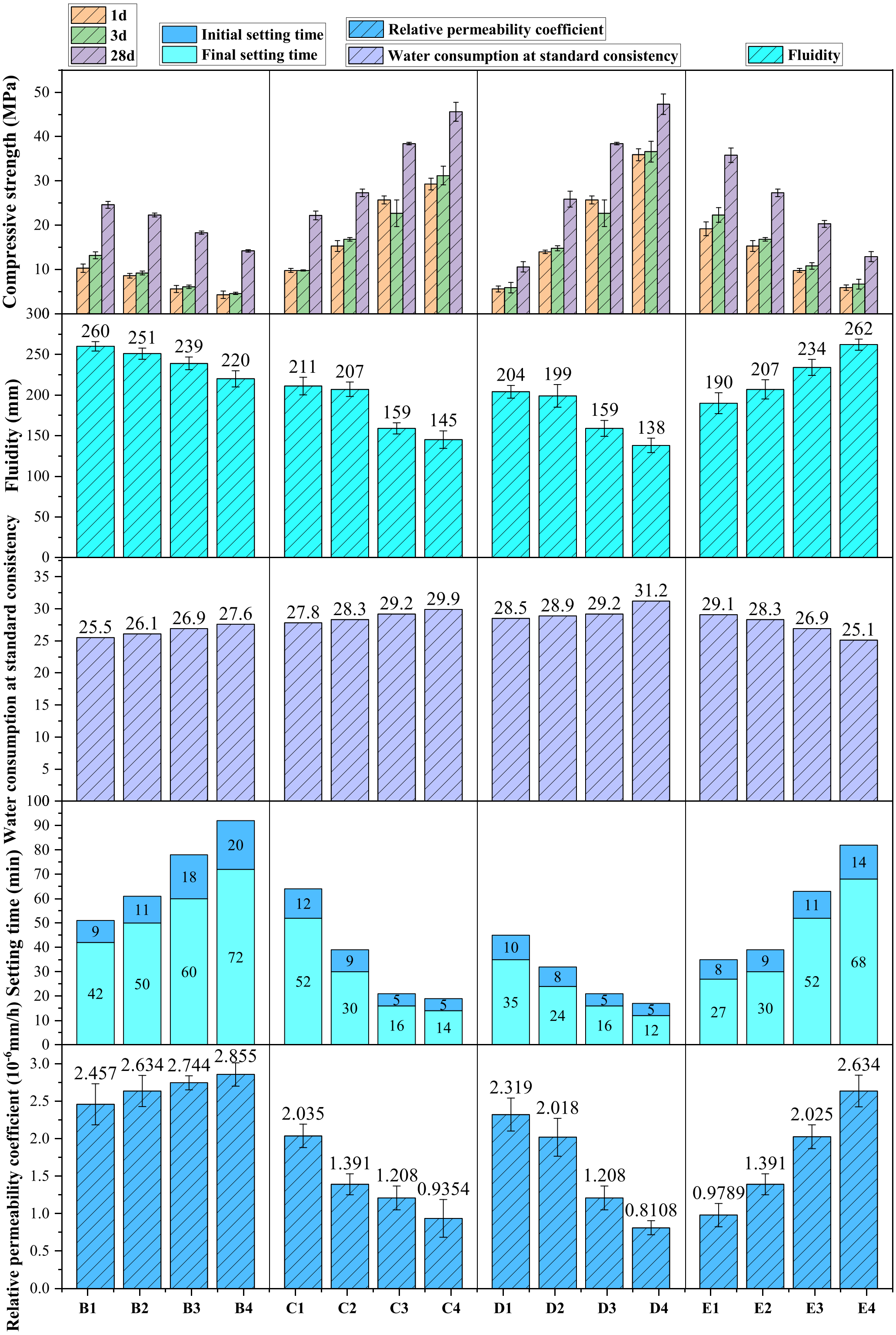

Fig. 4. Fluidity, setting time, water consumption, strength and permeability of all samples.

strength development of the samples over time. For the compressive strength tests, a WDW-10 C testing machine was used. The samples were subjected to a load at a rate of 2400 N/s to test their compressive strength. To eliminate accidental errors, strength tests were performed six times for each group.

The permeability tests were conducted in accordance with the Chinese standard DL/T 5150–2017. The samples used for the permeability test had dimensions of 80 mm, 70 mm, and 30 mm in diameter at the bottom, top, and height, respectively. To test the permeability, 3 samples need to be prepared for each group. The SS-15 mortar permeability tester was employed for the permeability tests. The test procedure involved applying pressure to the sample. Initially, the pressure was set at 0.2 MPa and maintained for a duration of 1 h. Subsequently, the pressure was increased by 0.1 MPa every hour. When the pressure reached 1.5 MPa and was sustained for 1 h, the sample would split, and the seepage height was measured.

2.3.2. *Microstructural analysis*

SEM and EDS were used to analyse the samples to measure the microstructure of the RUFA-RM-GGBS composite. SEM images were employed to study the microstructure and chemical composition of the RUFA-RM-GGBS composite. After the compressive strength test, a sample was selected from the broken sample for electron microscope analysis. To halt the hydration reaction, the internal parts of the crushed sample were immersed in anhydrous ethanol. Subsequently, the samples were placed in a drying oven and kept at a temperature of 60 °C for a period of 48 h. The bottom surface of the sample was then sanded using sandpaper to achieve a smooth and flat surface, which is more suitable for SEM/EDS analysis. Since the samples in this study were non-conductive, a thin layer of metallic platinum was applied to the surface of the samples. This platinum coating improves the sample's conductivity, allowing for accurate analysis using SEM/EDS techniques. After the application of the platinum coating and the fixation process, the microscopic morphology of the samples was observed and analyzed.

3. Results and discussion

3.1. *Effect of the partial replacement of RUFA by RM*

Fig. 4 displays the results of various tests conducted to evaluate the water consumption at standard consistency, fluidity, setting time, permeability, and strength of all samples. The influence of the replacement of RUFA by RM on the macroscopic properties of the composite based on RUFA was investigated. The analysis of water consumption at standard consistency revealed that as RM was introduced into the composite, the water consumption increased. Specifically, when the RM content was raised from 0% to 30%, the water consumption experienced an elevation of 8.2%. This is due to the small particle size of RM, which makes it require a large amount of water.

The fluidity of the composite is significantly influenced by the incorporation of RM. The test results indicate that the addition of RM leads to a reduction in the fluidity of the RUFA-based composite. This can be attributed to the flaky nature and high surface texture of RM particles, which can be seen in the SEM image of RM as shown in Fig. 2. In contrast, RUFA consists of regular spherical particles, which promote improved fluidity in the slurry. It is worth noting that even though the B4 group, which has the highest RM content, exhibits the lowest fluidity among the tested groups, its fluidity is still slightly higher than that of the control group. This is mainly due to the positive contribution of RUFA to fluidity.

The RUFA-RM slurry exhibits a short setting time, which is typical for alkali-activated materials. In the case of a geopolymer composed entirely of RUFA, the initial and final setting times are as short as 42 min and 51 min, respectively. This rapid setting is consistent with the characteristics of alkali-activated materials and can be attributed to the heat released during the reaction between the solid alkali activator and water [50]. However, this rapid setting behavior may not be ideal for grouting applications, where a longer working time is desirable. By incorporating RM into the composite, the setting time is prolonged. This indicates that RM can enhance the workability of the RUFA-based composite, which is consistent with the results found by Zhang et al. [51] and Ge et al. [52]. This is because RM has lower reactivity compared to RUFA [53]. The lower reactivity of RM slows down the rate of hydration reactions, thereby extending the setting time of the composite. As the content of RM increases from 0% to 30%, both the initial and final setting times increase significantly by 71.4% and 122.2%, respectively.

Based on the strength test results, the compressive strength of the composite based on RUFA ranges from 14.2 MPa to 24.6 MPa after 28 days of curing. However, when compared to the control group, the compressive strength of the RUFA-RM composite was significantly lower. This decrease in strength can be attributed to the incorporation of RM, which reduces the compressive strength of the RUFA-based composite. One possible explanation for this phenomenon is the low activity of RM, which leads to a loose structure in the material. In contrast, C-A-S-H gels play a vital role in contributing to the strength of the composite, and they are the main hydration product of geopolymer [54]. The addition of RM can hinder the production of C-A-S-H gel, thereby reducing the strength of the RUFA-based composite. Compressive strength is a crucial parameter in engineering, as it determines the overall quality of the structure. Therefore, it is important to limit the content of RM to prevent excessive loss of strength.

Permeability tests have revealed that the inclusion of RM in the RUFA-based composite leads to an increase in permeability. This outcome suggests that the addition of RM causes the structure of the composite to become looser, aligning with the earlier findings related to strength. Consequently, it is advisable to restrict the content of RM to enhance both mechanical strength and fluidity of the composite. Furthermore, it is essential to acknowledge the positive impact of RM on the initial and final setting time of the RUFA-based composite. The incorporation of RM can influence the setting time, allowing for more control over the curing process. This aspect should be considered when determining the optimal content of RM for achieving the desired setting characteristics.

In summary, limiting the amount of RM in the composite is recommended to maintain better mechanical strength, improve fluidity, and regulate the setting time of the RUFA-based composite.

3.2. *Effect of the partial replacement of RUFA/RM by GGBS*

Two methods for incorporating GGBS into RUFA/RM-based composites are commonly employed: partial replacement of RUFA with GGBS and partial replacement of RM with GGBS. The selection of these methods leads to variations in the performance of RUFA/RM/GGBS-based composites. In order to investigate the impact of partial replacement of RUFA/RM with GGBS, ternary composite samples were prepared, wherein RUFA or RM was substituted with varying amounts of GGBS. Subsequently, tests were conducted to evaluate the fluidity, initial and final setting time, and compressive strength of the samples.

The results of water consumption at standard consistency show that as the content of GGBS increases, the water consumption of the composite also increases.

The fluidity test results indicate that the inclusion of GGBS in the RUFA/RM/GGBS-based composite leads to a reduction in fluidity. This finding aligns with the observations made in Zhang's study [55]. Unlike the regular spherical shape of RUFA particles, GGBS particles have an irregular shape, which unfavorably affects the flowability of the slurry. When the GGBS content reaches 10%, the fluidity of the composite becomes similar to that of cement compared to the control group. However, with a GGBS content of 40%, the fluidity of the composite is only around 63–66% of that of the control group. Furthermore, the results obtained from Groups B and C indicate a negative correlation between the content of RM and GGBS and the fluidity of the RUFA/RM/GGBS-based composite. Additionally, the findings from Group D demonstrate that the influence of GGBS on fluidity is greater than that of RM. This disparity can be attributed to the irregular shape of GGBS particles and the higher CaO content present in GGBS compared to RM. Moreover, the issue of flash setting, which refers to the rapid setting of alkali-activated materials, is associated with the presence of CaO [56]. This rapid setting phenomenon leads to a decrease in fluidity.

The setting time test results reveal that incorporating GGBS through partial replacement of RUFA or RM leads to a reduction in both the initial and final setting times of the RUFA/RM/GGBS-based composite. This outcome suggests that the presence of a substantial amount of CaO in GGBS promotes hydration reactions within the composite.

The compressive strength test results indicate that the partial replacement of RUFA or RM with GGBS results in an increase in the compressive strength of the RUFA/RM/GGBS-based composite, particularly in the early stages of curing. This trend corresponds with the findings presented in Alam's [57] study as well. Remarkably, when the GGBS content reaches 30%, the compressive strength of the composite after just one day of curing surpasses that of the control group. This improvement in compressive strength can be attributed to the rapid synthesis of calcium alumino-silicate hydrate (C-A-S-H) gels facilitated by the presence of Ca^{2+} ions available in GGBS [58].

The results of permeability tests demonstrate that the inclusion of GGBS in the RUFA-based composite leads to a reduction in permeability. This effect can be attributed to the promotion of C-A-S-H gel synthesis facilitated by the incorporation of GGBS. C-A-S-H gels possess a strong filling capacity, resulting in a more compact structure of the composite. As a result, the permeability of the composite decreases.

In summary, the addition of sufficient GGBS is crucial for achieving high compressive strength in the RUFA/RM/GGBS-based composite. However, it is important to address potential drawbacks associated with large amounts of GGBS, such as the occurrence of flash setting and reduced fluidity. These issues should not be overlooked and must be carefully managed during the composite production process.

3.3. *Effect of S/B*

The amount of water plays a significant role in determining the properties of the RUFA/RM/GGBS-based composite. According to the results obtained from the water consumption test at standard consistency, a negative correlation is observed between the S/B (Solid/Binder) ratio and water consumption at standard consistency.

Furthermore, the fluidity test results reveal that increasing the S/B ratio enhances the fluidity of the RUFA/RM/GGBS-based composite. This improvement in fluidity can be attributed to the higher S/B ratio, which results in an increased amount of free water within the slurry. The presence of free water reduces the interaction and internal friction between the constituent particles of the composite [59,60]. Consequently, a higher S/B ratio promotes better fluidity in the slurry.

The S/B ratio has a significant impact on the setting time of the RUFA/RM/GGBS-based composite. Increasing the S/B ratio leads to a reduction in the concentration of silica and aluminum ions in the composite mixture, resulting in prolonged initial and final setting times. The setting time of the composite is influenced by various factors, including the depolymerization and polycondensation of precursors. These processes require a highly alkaline environment. However, when the S/B ratio increases, the concentration of OH-ions, which are produced by the hydrolysis of the alkaline activator, becomes diluted. This dilution weakens the alkaline environment within the RUFA/RM/GGBS-based composite. As a result, the initial and final setting times of the composite are prolonged.

However, The S/B ratio exhibits a negative relationship with the compressive strength of the RUFA/RM/GGBS-based composite, which is consistent with previous findings in the field of alkali-activated materials [61]. Excess water content in the composite negatively affects its strength because it hinders the hydration process [62]. Additionally, as the S/B ratio increases, the porosity of the composite also increases, further reducing its mechanical strength. However, excessive water content can even prevent the composite from properly shaping and developing strength.

Furthermore, the permeability of the RUFA/RM/GGBS-based composite decreases as the S/B ratio increases. This is because during the process of mechanical strength formation, excess water gradually evaporates, increasing the internal porosity of the material, and subsequently increasing its permeability.

In summary, an increase in the S/B ratio can improve the fluidity of the composite and prolong the initial and final setting times.

3.4. SEM-EDS analyses

SEM images of the RUFA/RM/GGBS-based composite at different magnifications are shown in Fig. 5. The images clearly depict a relatively dense matrix in all the samples. However, it is noteworthy that some incompletely reacted RUFA particles and microcracks can also be observed. The reaction products exhibit a dense packing around the RUFA particles that have not yet undergone complete reaction, indicating the composite's high reactivity to polycondensation. Microcracks are typically concentrated around the unreacted RUFA particles, and while they may have resulted from the crushing process during sample preparation, these particles themselves can be vulnerable areas that contribute to the formation of microcracks. Additionally, the appearance of these microcracks may be associated with the phenomenon of dry shrinkage commonly observed in alkali-activated materials. Although they may have been a result of the crushing process, these particles can easily be the weak part that causes these microcracks to form. the emergence of microcracks could also be linked to the dry shrinkage behavior observed in alkali-activated materials.

Furthermore, the SEM images depict the existence of air voids or gaps within the composite material, ranging in size from 5 to 50 μm. These gaps may be attributed to the introduction of air bubbles during the mixing process or the evaporation of excess water. Notably, as the GGBS content increases, the size of the gaps tends to decrease. This phenomenon provides an explanation for the observed increase in compressive strength and impermeability with higher GGBS content. Moreover, the variation in GGBS content influences the gel type present in the samples. At relatively low GGBS content and high RUFA content, the predominant gel type is N-A-S-H (sodium aluminosilicate hydrate) [44]. However, as the GGBS content increases, the N-A-S-H gel gradually gives way to C-A-S-H (calcium aluminosilicate hydrate). In other words, sodium ions (Na^+) are gradually replaced by calcium ions (Ca^{2+}). C-A-S-H gels exhibit higher strength and greater filling capacity [63,64]. This change in gel type is also evident in the results of energy-dispersive EDS. The Si/Ca ratio of sample C1, with low GGBS content, is approximately half that of sample C3, indicating the dominance of N-A-S-H gels in C1 [65]. However, in sample C3, with high GGBS content, N-A-S-H gels are replaced by C-A-S-H gels, because N-A-S-H gels are unlikely to dominate the gel phase in systems with a high calcium content [66]. The synthesis of this gel increases the thickness of the composite structure and thereby enhances its strength. Additionally, based on the data and previous research [67–70], the SEM images also reveal the presence of various hydration products such as C-S-H, CH, and Aft, further confirming the progress of the

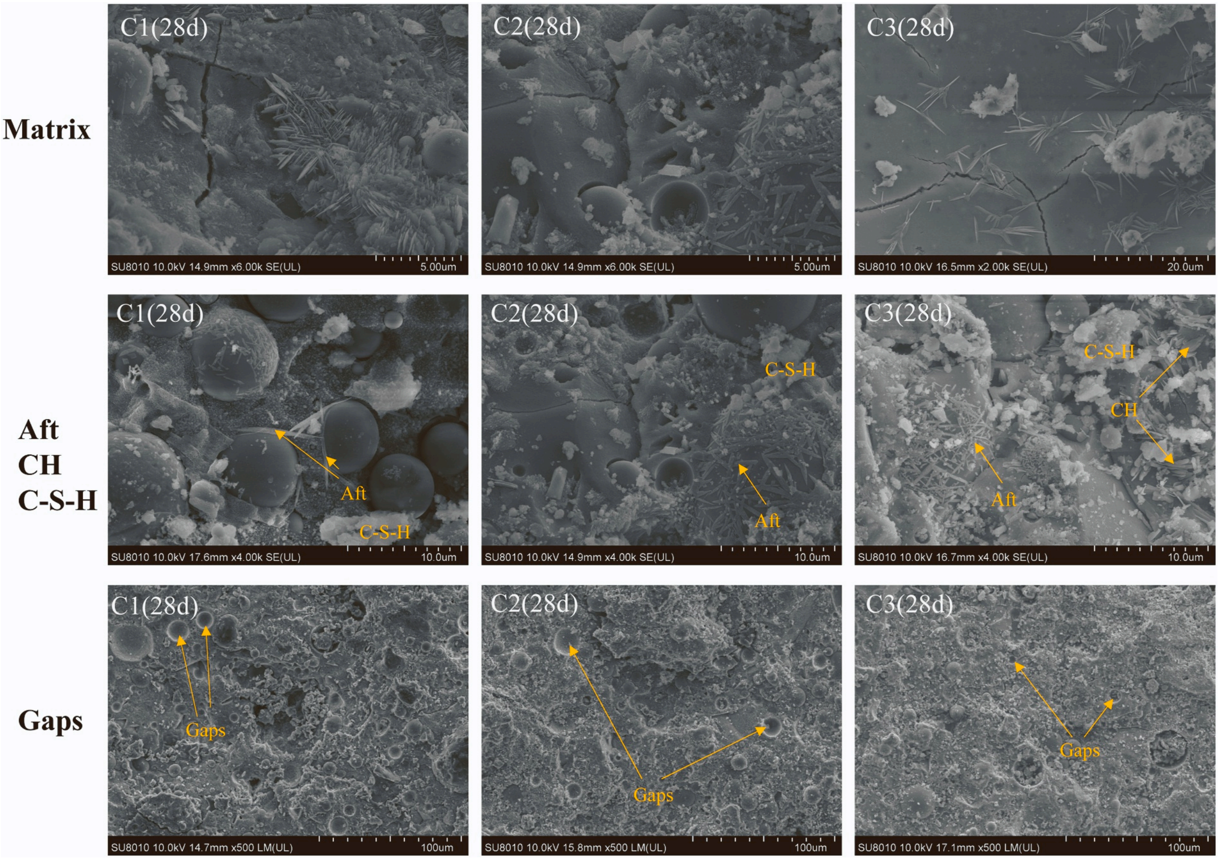

Fig. 5. SEM analysis of the samples (C1, C2 and C3 curing at 28d).

hydration process within the samples.

To investigate the constituent elements of the reaction products, EDS analysis was carried out on these RUFA/RM/GGBS composites, as shown in Fig. 6. The colors represent the spatial distribution of these elements. The EDS analysis reveals the presence of several elements including C, O, Na, Al, Si, Ca, and Fe within the sample cross-section, as illustrated in Fig. 6. Among these elements, the predominant contribution of Ca is attributed to the presence of GGBS, which participates in the formation of C-A-S-H gel, thereby enhancing the overall strength of the composite. Al and Si are both constituent elements of geopolymers, playing a crucial role in the formation of the composite structure.

3.5. Sustainability analysis

In the pursuit of RM-based ecological cementless composites, an assessment of greenhouse gas (GHG) emissions was conducted to compare them with normal cement paste. The GHG emissions associated with cement production are primarily generated during its manufacturing process [71]. China, being the world's leading cement producer, accounts for more than 60% of global production [72]. In 2021, the production of 1 metric ton of cement resulted in high CO_2 emissions of 780 metric tons, indicating a specific emission rate of 0.78 kg CO_2/kg [73–75]. Similarly, the GHG emissions for other composite ingredients including RUFA, RM, GGBS, NaOH, and SS can be estimated as 0.005, 0.303, 0.067, 3.2, and 0.4 kg CO_2/kg, respectively [73,75–77]. Notably, RM, as a solid waste with a significant quantity and high geopolymerization potential, exhibits only half the GHG emissions compared to cement. This further emphasizes its substantial sustainability value in geopolymer production. The specific CO_2 emissions for the various mixture ingredients are summarized in Table 3.

The GHG emissions for conventional cement paste and ecological cementless composites were calculated based on a consistent volume of 1 m^3, and the results are presented in Table 4. The reduction index, which indicates the extent of GHG emission reduction compared to a reference mixture (A0), was calculated by subtracting the GHG emission of a specific mixture from that of A0 and dividing the result by the GHG emission of A0. The highest reduction index of 0.66 was achieved by mixture B2, indicating that it represents the best ecological and sustainable RM-based mixture design. Taking into account the comprehensive properties discussed earlier, the final mixture design can be determined by considering multiple factors. It is worth noting that all the mixtures in this study exhibited a reduction index higher than 0.5, confirming the effectiveness of the introduced ternary cementless composite in significantly reducing GHG emissions by eliminating the use of cement.

4. Conclusions

In this study, a ternary cementless composite was formulated by combining RM, RUFA, and GGBS. The properties analyzed included water consumption at standard consistency, fluidity, initial and final setting times, permeability, and compressive strength. Based on the results obtained from the comparative analysis, the following conclusions can be drawn:

(1) The addition of RM to the RUFA/RM/GGBS cementless composite resulted in increased water consumption at standard consistency and permeability. This also led to reduced fluidity and compressive strength, as well as prolonged setting times.
(2) The incorporation of GGBS in RUFA/RM/GGBS cementless composites yields significant benefits, including higher compressive strength and reduced permeability. However, the addition of GGBS also presents certain challenges, notably flash setting, which results in prolonged setting times, diminished fluidity, and increased water consumption at standard consistency.
(3) In the RUFA/RM/GGBS cementless composite, various hydration products were observed, including C-S-H, Aft, CH, N-A-S-H, and C-A-S-H gels. The composition of these hydration products was found to be influenced by the content of GGBS. Specifically, when the GGBS content was lower, there was a preference for the presence of N-A-S-H gels. However, with higher GGBS content, some of the N-A-S-H gels were replaced by C-A-S-H gels. This indicates that the proportion of GGBS in the composite has a direct impact on the type of gels formed during the hydration process.
(4) Indeed, with the increase in GGBS content, the composite exhibited smaller microcracks. This phenomenon played a crucial role in enhancing the compressive strength of the material and concurrently reducing its permeability. The smaller microcracks contributed to a more compact and denser structure, ultimately leading to improved mechanical properties and a decreased tendency for fluid or other substances to permeate through the material.
(5) The greenhouse gas emissions of all the mixtures in this study are much lower than those of cement. Mixture E4 has only 36% of the greenhouse gas emissions of cement. This emphasizes the substantial sustainability value of the RUFA/RM/GGBS cementless composite in geopolymer production.

Declaration of Competing Interest

The authors declare that they have no known competing financial interests or personal relationships that could have appeared to influence the work reported in this paper.

Data Availability

Data will be made available on request.

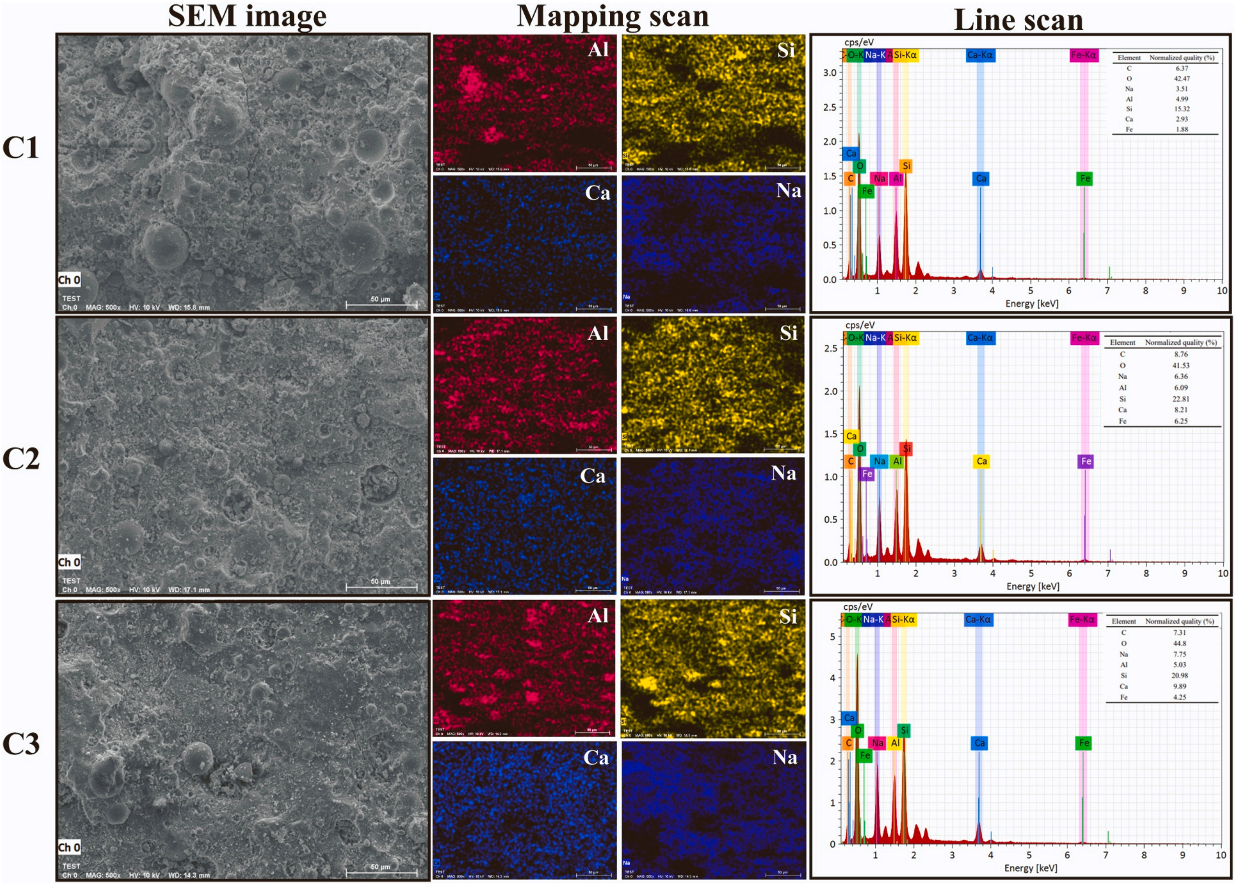

Fig. 6. EDS mapping and line scan of the samples (C1, C2 and C3 curing at 28d).

Table 3
The specific CO_2 emissions (kg CO_2e/kg) for various mixture ingredients.

PC[73,75]	RUFA[77]	RM[76]	GGBS[77]	NaOH[73,75]	SS[73,75]
0.780	0.005	0.303	0.067	3.2	0.4

Table 4
The GHG emissions for mixture designs based on the consistent volume of 1 m^3.

Mixture notation	PC-RUFA-RM-GGBS (%)	S/B	CO_2 (kg/m^3)	Reduction index
B1	0–100–0–0	0.45	296.75	0.70
B2	0–90–10–0	0.45	339.94	0.66
B3	0–80–20–0	0.45	384.32	0.61
B4	0–70–30–0	0.45	429.94	0.57
C1	0–70–20–10	0.45	395.26	0.60
C2	0–60–20–20	0.45	406.34	0.59
C3	0–50–20–30	0.45	417.57	0.58
C4	0–40–20–40	0.45	428.96	0.57
D1	0–50–40–10	0.45	488.74	0.51
D2	0–50–30–20	0.45	452.90	0.55
D3	0–50–20–30	0.45	417.57	0.58
D4	0–50–10–40	0.45	382.74	0.62
E1	0–60–20–20	0.4	435.74	0.56
E2	0–60–20–20	0.45	406.34	0.59
E3	0–60–20–20	0.5	380.65	0.62
E4	0–60–20–20	0.55	358.02	0.64
A0	100–0–0–0	0.45	995.74	0

Acknowledgements

The authors gratefully acknowledge the financial supports received from the National Natural Science Foundation of China (Grant Nos. 12172130) and the Key Research and Development Program of Jiangxi Province (Grant Nos. 20212BBE53016, 20202ACBL214016, 20212BDH81034, 20224BAB204074, GJJ210626).

References

[1] S.M.A. Qaidi, B.A. Tayeh, H.U. Ahmed, W. Emad, A review of the sustainable utilisation of red mud and fly ash for the production of geopolymer composites, Constr. Build. Mater. 350 (2022), 128892, https://doi.org/10.1016/j.conbuildmat.2022.128892.

[2] X. Teng, J. Li, J. Wang, J. Liu, X. Ge, T. Gu, Effective degradation of atrazine in wastewater by three-dimensional electrochemical system using fly ash-red mud particle electrode: mechanism and pathway, Sep. Purif. Technol. 267 (2021), 118661, https://doi.org/10.1016/j.seppur.2021.118661.

[3] P. Gill, P. Jangra, R. Roychand, M. Saberian, J. Li, Effects of various additives on the crumb rubber integrated geopolymer concrete, Clean. Mater. 8 (2023), 100181, https://doi.org/10.1016/j.clema.2023.100181.

[4] X. Liu, Y. Han, F. He, P. Gao, S. Yuan, Characteristic, hazard and iron recovery technology of red mud - A critical review, J. Hazard. Mater. 420 (2021), 126542, https://doi.org/10.1016/j.jhazmat.2021.126542.

[5] M. Muraleedharan, Y. Nadir, Factors affecting the mechanical properties and microstructure of geopolymers from red mud and granite waste powder: a review, Ceram. Int. 47 (10, Part A) (2021) 13257–13279, https://doi.org/10.1016/j.ceramint.2021.02.009.

[6] W. Ruan, J. Liao, J. Mo, F. Li, X. Gu, Y. Ma, Y. Zhu, X. Ma, Effects of red mud on properties of magnesium phosphate cement-based grouting material and its bonding mechanism with coal rock, Ceram. Int. 49 (2) (2023) 2015–2025, https://doi.org/10.1016/j.ceramint.2022.09.167.

[7] J. Shi, X. Guan, J. Ming, X. Zhou, Improved corrosion resistance of reinforcing steel in mortars containing red mud after long-term exposure to aggressive environments, Cem. Concr. Compos. 130 (2022), 104522, https://doi.org/10.1016/j.cemconcomp.2022.104522.

[8] S. Vigneshwaran, M. Uthayakumar, V. Arumugaprabu, Potential use of industrial waste-red mud in developing hybrid composites: a waste management approach, J. Clean. Prod. 276 (2020), 124278, https://doi.org/10.1016/j.jclepro.2020.124278.

[9] N. Yao, X. Zhou, Y. Liu, J. Shi, Synergistic effect of red mud and fly ash on passivation and corrosion resistance of 304 stainless steel in alkaline concrete pore solutions, Cem. Concr. Compos. 132 (2022), 104637, https://doi.org/10.1016/j.cemconcomp.2022.104637.

[10] F. Lyu, Y. Hu, L. Wang, W. Sun, Dealkalization processes of bauxite residue: a comprehensive review, J. Hazard. Mater. 403 (2021), 123671, https://doi.org/10.1016/j.jhazmat.2020.123671.

[11] Y. Hua, K.V. Heal, W. Friesl-Hanl, The use of red mud as an immobiliser for metal/metalloid-contaminated soil: a review, J. Hazard. Mater. 325 (2017) 17–30, https://doi.org/10.1016/j.jhazmat.2016.11.073.

[12] E. Mukiza, L. Zhang, X. Liu, N. Zhang, Utilization of red mud in road base and subgrade materials: a review, Resour., Conserv. Recycl. 141 (2019) 187–199, https://doi.org/10.1016/j.resconrec.2018.10.031.

[13] S. Agrawal, N. Dhawan, Evaluation of red mud as a polymetallic source – A review, Miner. Eng. 171 (2021), 107084, https://doi.org/10.1016/j.mineng.2021.107084.

[14] F. Aslani, J.B. Sun, D. Bromley, G.W. Ma, Fiber-reinforced lightweight self-compacting concrete incorporating scoria aggregates at elevated temperatures, Struct. Concr. 20 (3) (2019) 1022–1035, https://doi.org/10.1002/suco.201800231.

[15] M. Wang, X. Liu, Applications of red mud as an environmental remediation material: a review, J. Hazard. Mater. 408 (2021), 124420, https://doi.org/10.1016/j.jhazmat.2020.124420.

[16] B.B. Yin, W.K. Sun, Y. Zhang, K.M. Liew, Modeling via peridynamics for large deformation and progressive fracture of hyperelastic materials, Comput. Methods Appl. Mech. Eng. 403 (2023), 115739, https://doi.org/10.1016/j.cma.2022.115739.

[17] J. Obeng, A. Andrews, M. Adom-Asamoah, S. Adjei, Effect of calcium carbide residue on the sulphate resistance of metakaolin-based geopolymer mortars, Clean. Mater. 7 (2023), 100177, https://doi.org/10.1016/j.clema.2023.100177.

[18] F. Aslani, J.B. Sun, G.Q. Huang, Mechanical behavior of fiber-reinforced self-compacting rubberized concrete exposed to elevated temperatures, J. Mater. Civ. Eng. 31 (12) (2019), https://doi.org/10.1061/(ASCE)MT.1943-5533.0002942.

[19] X.D. Ou, S.J. Chen, J. Jiang, J.X. Qin, Z.J. Tan, Analysis of engineering characteristics and microscopic mechanism of red mud-bauxite tailings mud foam light soil, Materials 15 (5) (2022), https://doi.org/10.3390/ma15051782.

[20] S. Xue, W. Ke, F. Zhu, Y. Ye, Z. Liu, J. Fan, W. Hartley, Effect of phosphogypsum and poultry manure on aggregate-associated alkaline characteristics in bauxite residue, J. Environ. Manag. 256 (2020), 109981, https://doi.org/10.1016/j.jenvman.2019.109981.

[21] B.B. Yin, A. Akbar, Y. Zhang, K.M. Liew, Modeling progressive failure and crack evolution in a randomly distributed fiber system via a coupled phase-field cohesive model, Compos. Struct. 313 (2023), 116959, https://doi.org/10.1016/j.compstruct.2023.116959.

[22] K. Zhou, C. Teng, X. Zhang, C. Peng, W. Chen, Enhanced selective leaching of scandium from red mud, Hydrometallurgy 182 (2018) 57–63, https://doi.org/10.1016/j.hydromet.2018.10.011.

[23] M.A. Khairul, J. Zanganeh, B. Moghtaderi, The composition, recycling and utilisation of Bayer red mud, Resour., Conserv. Recycl. 141 (2019) 483–498, https://doi.org/10.1016/j.resconrec.2018.11.006.

[24] M.D. Hoang, Q.M. Do, V.Q. Le, Effect of curing regime on properties of red mud based alkali activated materials, Constr. Build. Mater. 259 (2020), 119779, https://doi.org/10.1016/j.conbuildmat.2020.119779.

[25] J. Zhang, S.C. Li, Z.F. Li, C. Liu, Y.F. Gao, Feasibility study of red mud for geopolymer preparation: effect of particle size fraction, J. Mater. Cycles Waste Manag. 22 (5) (2020) 1328–1338, https://doi.org/10.1007/s10163-020-01023-4.

[26] P. Wang, D.Y. Liu, Physical and chemical properties of sintering red mud and bayer red mud and the implications for beneficial utilization, Materials 5 (10) (2012) 1800–1810, https://doi.org/10.3390/ma5101800.

[27] W. Hu, Q. Nie, B. Huang, X. Shu, Q. He, Mechanical and microstructural characterization of geopolymers derived from red mud and fly ashes, J. Clean. Prod. 186 (2018) 799–806, https://doi.org/10.1016/j.jclepro.2018.03.086.

[28] F. Blanco, M.P. Garcia, J. Ayala, G. Mayoral, M.A. Garcia, The effect of mechanically and chemically activated fly ashes on mortar properties, Fuel 85 (14) (2006) 2018–2026, https://doi.org/10.1016/j.fuel.2006.03.031.

[29] J. Vargas, A. Halog, Effective carbon emission reductions from using upgraded fly ash in the cement industry, J. Clean. Prod. 103 (2015) 948–959, https://doi.org/10.1016/j.jclepro.2015.04.136.

[30] P. Kara De Maeijer, B. Craeye, R. Snellings, H. Kazemi-Kamyab, M. Loots, K. Janssens, G. Nuyts, Effect of ultra-fine fly ash on concrete performance and durability, Constr. Build. Mater. 263 (2020), 120493, https://doi.org/10.1016/j.conbuildmat.2020.120493.

[31] W. Lin, Development of cementless binder for low thermal conductivity materials: reactive ultra-fine fly ash mixed with co-fired fly ash, Case Stud. Constr. Mater. 16 (2022), e899, https://doi.org/10.1016/j.cscm.2022.e00899.

[32] W. Lin, Reactive ultra-fine fly ash as an additive for cement-based materials, Mater. Today Commun. 25 (2020), 101466, https://doi.org/10.1016/j.mtcomm.2020.101466.

[33] K. Chen, W. Lin, W. Liu, Effect of NaOH concentration on properties and microstructure of a novel reactive ultra-fine fly ash geopolymer, Adv. Powder Technol. 32 (8) (2021) 2929–2939, https://doi.org/10.1016/j.apt.2021.06.008.

[34] Z. Yang, R. Mocadlo, M. Zhao, R.D. Sisson, M. Tao, J. Liang, Preparation of a geopolymer from red mud slurry and class F fly ash and its behavior at elevated temperatures, Constr. Build. Mater. 221 (2019) 308–317, https://doi.org/10.1016/j.conbuildmat.2019.06.034.

[35] H. Choo, S. Lim, W. Lee, C. Lee, Compressive strength of one-part alkali activated fly ash using red mud as alkali supplier, Constr. Build. Mater. 125 (2016) 21–28, https://doi.org/10.1016/j.conbuildmat.2016.08.015.

[36] F. Aslani, L.J. Hou, S. Nejadi, J.B. Sun, S. Abbasi, Experimental analysis of fiber-reinforced recycled aggregate self-compacting concrete using waste recycled concrete aggregates, polypropylene, and steel fibers, Struct. Concr. 20 (5) (2019) 1670–1683, https://doi.org/10.1002/suco.201800336.

[37] Y. Bian, Z. Li, J. Zhao, Y. Wang, Synergistic enhancement effect of recycled fine powder (RFP) cement paste and carbonation on recycled aggregates performances and its mechanism, J. Clean. Prod. 344 (2022), 130848, https://doi.org/10.1016/j.jclepro.2022.130848.

[38] J.W. Li, Q.R. Qin, J.B. Sun, Y.Z. Ma, Q. Li, Mechanical and conductive performance of electrically conductive cementitious composite using graphite, steel slag, and GGBS, Struct. Concr. 23 (1) (2022) 533–547, https://doi.org/10.1002/suco.202000617.

[39] L.G. Li, J.Y. Zheng, J. Zhu, A.K.H. Kwan, Combined usage of micro-silica and nano-silica in concrete: SP demand, cementing efficiencies and synergistic effect, Constr. Build. Mater. 168 (2018) 622–632, https://doi.org/10.1016/j.conbuildmat.2018.02.181.

[40] Y. Shi, H. Jing, B. Liu, C. Hou, H. Qian, Synergistic utilization of porous coral sand and fly ash for multifunctional engineered cementitious composites with polyethylene fibers: intensified electromagnetic wave absorption and mechanism, J. Clean. Prod. 396 (2023), 136497, https://doi.org/10.1016/j.jclepro.2023.136497.

[41] J. Sun, F. Aslani, J. Wei, X. Wang, Electromagnetic absorption of copper fiber oriented composite using 3D printing, Constr. Build. Mater. 300 (2021), 124026, https://doi.org/10.1016/j.conbuildmat.2021.124026.

[42] J. Sun, Y. Wang, K. Li, X. Yao, B. Zhu, J. Wang, Q. Dong, X. Wang, Molecular interfacial properties and engineering performance of conductive fillers in cementitious composites, J. Mater. Res. Technol. 19 (2022) 591–604, https://doi.org/10.1016/j.jmrt.2022.05.061.

[43] Y. Tang, Z. Huang, Z. Chen, M. Chen, H. Zhou, H. Zhang, J. Sun, Novel visual crack width measurement based on backbone double-scale features for improved detection automation, Eng. Struct. 274 (2023), 115158, https://doi.org/10.1016/j.engstruct.2022.115158.

[44] K. Chen, W. Lin, Q. Liu, B. Chen, V.W.Y. Tam, Micro-characterizations and geopolymerization mechanism of ternary cementless composite with reactive ultra-fine fly ash, red mud and recycled powder, Constr. Build. Mater. 343 (2022), 128091, https://doi.org/10.1016/j.conbuildmat.2022.128091.

[45] M. P, V. V, Potential utilization of waste glass powder as a precursor material in synthesizing ecofriendly ternary blended geopolymer matrix, J. Clean. Prod. 355 (2022), 131860, https://doi.org/10.1016/j.jclepro.2022.131860.

[46] J. Sun, S. Lin, G. Zhang, Y. Sun, J. Zhang, C. Chen, A.M. Morsy, X. Wang, The effect of graphite and slag on electrical and mechanical properties of electrically conductive cementitious composites, Constr. Build. Mater. 281 (2021), 122606, https://doi.org/10.1016/j.conbuildmat.2021.122606.

[47] J. Sun, Y. Tang, J. Wang, X. Wang, J. Wang, Z. Yu, Q. Cheng, Y. Wang, A multi-objective optimisation approach for activity excitation of waste glass mortar, J. Mater. Res. Technol. 17 (2022) 2280–2304, https://doi.org/10.1016/j.jmrt.2022.01.066.

[48] J. Sun, Y. Wang, S. Liu, A. Dehghani, X. Xiang, J. Wei, X. Wang, Mechanical, chemical and hydrothermal activation for waste glass reinforced cement, Constr. Build. Mater. 301 (2021), 124361, https://doi.org/10.1016/j.conbuildmat.2021.124361.

[49] E.A. Taye, J.A. Roether, D.W. Schubert, D.T. Redda, A.R. Boccaccini, Hemp fiber reinforced red Mud/Fly ash geopolymer composite materials: effect of fiber content on mechanical strength, Materials 14 (3) (2021), https://doi.org/10.3390/ma14030511.

[50] S.Y. Oderji, B. Chen, C. Shakya, M.R. Ahmad, S.F.A. Shah, Influence of superplasticizers and retarders on the workability and strength of one-part alkali-activated fly ash/slag binders cured at room temperature, Constr. Build. Mater. 229 (2019), 116891, https://doi.org/10.1016/j.conbuildmat.2019.116891.

[51] J. Zhang, S. Li, Z. Li, C. Liu, Y. Gao, Y. Qi, Properties of red mud blended with magnesium phosphate cement paste: Feasibility of grouting material preparation, Constr. Build. Mater. 260 (2020), 119704, https://doi.org/10.1016/j.conbuildmat.2020.119704.

[52] X. Ge, X. Hu, C. Shi, Mechanical properties and microstructure of circulating fluidized bed fly ash and red mud-based geopolymer, Constr. Build. Mater. 340 (2022), 127599, https://doi.org/10.1016/j.conbuildmat.2022.127599.

[53] S. Vigneshwaran, M. Uthayakumar, V. Arumugaprabu, Development and sustainability of industrial waste-based red mud hybrid composites, J. Clean. Prod. 230 (2019) 862–868, https://doi.org/10.1016/j.jclepro.2019.05.131.

[54] P.D. Silva, K. Sagoe-Crenstil, V. Sirivivatnanon, Kinetics of geopolymerization: role of Al2O3 and SiO2, Cem. Concr. Res. 37 (4) (2007) 512–518, https://doi.org/10.1016/j.cemconres.2007.01.003.

[55] L.C. Zhang, X.N. Jia, C. Wang, Q.G. Jiang, C.Q. Sun, Characterization of magnesium potassium phosphate cement-based grouting material blended with high volume industrial wastes, Adv. Mater. Sci. Eng. 2022 (2022), https://doi.org/10.1155/2022/7353985.

[56] T. Revathi, R. Jeyalakshmi, Fly ash–GGBS geopolymer in boron environment: a study on rheology and microstructure by ATR FT-IR and MAS NMR, Constr. Build. Mater. 267 (2021), 120965, https://doi.org/10.1016/j.conbuildmat.2020.120965.

[57] S. Alam, S.K. Das, B.H. Rao, Strength and durability characteristic of alkali activated GGBS stabilized red mud as geo-material, Constr. Build. Mater. 211 (2019) 932–942, https://doi.org/10.1016/j.conbuildmat.2019.03.261.

[58] M. Palacios, P. Banfill, F. Puertas, Rheology and setting of alkali-activated slag pastes and mortars: effect of organ admixture, Acids Mater. J. 105 (2) (2008) 140–148.

[59] C. Jayasree, R. Gettu, Experimental study of the flow behaviour of superplasticized cement paste, Mater. Struct. 41 (9) (2008) 1581–1593, https://doi.org/10.1617/s11527-008-9350-5.

[60] Z. Zuhua, Y. Xiao, Z. Huajun, C. Yue, Role of water in the synthesis of calcined kaolin-based geopolymer, Appl. Clay Sci. 43 (2) (2009) 218–223, https://doi.org/10.1016/j.clay.2008.09.003.

[61] J. Xie, O. Kayali, Effect of initial water content and curing moisture conditions on the development of fly ash-based geopolymers in heat and ambient temperature, Constr. Build. Mater. 67 (2014) 20–28, https://doi.org/10.1016/j.conbuildmat.2013.10.047.

[62] C. Xu, Z. Zhang, X. Tang, Z. Gui, F. Liu, Synthesis and characterization of one-part alkali-activated grouting materials based on granulated blast furnace slag, uncalcined coal gangue and microscopic fly ash sinking beads, Constr. Build. Mater. 345 (2022), 128254, https://doi.org/10.1016/j.conbuildmat.2022.128254.

[63] X.W. Ouyang, Y.W. Ma, Z.Y. Liu, J.J. Liang, G. Ye, Effect of the sodium silicate modulus and slag content on fresh and hardened properties of alkali-activated fly ash/slag, Minerals 10 (1) (2020), https://doi.org/10.3390/min10010015.

[64] A. Rafeet, R. Vinai, M. Soutsos, W. Sha, Effects of slag substitution on physical and mechanical properties of fly ash-based alkali activated binders (AABs), Cem. Concr. Res. 122 (2019) 118–135, https://doi.org/10.1016/j.cemconres.2019.05.003.

[65] P. Ghadir, H.R. Razeghi, Effects of sodium chloride on the mechanical strength of alkali activated volcanic ash and slag pastes under room and elevated temperatures, Constr. Build. Mater. 344 (2022), 128113, https://doi.org/10.1016/j.conbuildmat.2022.128113.

[66] I. Garcia-Lodeiro, S. Donatello, A. Fernandez-Jimenez, A. Palomo, Hydration of hybrid alkaline cement containing a very large proportion of fly ash: a descriptive model, Materials 9 (7) (2016), https://doi.org/10.3390/ma9070605.

[67] X. Jiang, Y. Zhang, Y. Zhang, J. Ma, R. Xiao, F. Guo, Y. Bai, B. Huang, Influence of size effect on the properties of slag and waste glass-based geopolymer paste, J. Clean. Prod. 383 (2023), 135428, https://doi.org/10.1016/j.jclepro.2022.135428.

[68] B.B. Yin, G. Li, Y. Zhang, K.M. Liew, Sustainability-driven atomistic model for exploring the mechanical properties of low carbon limestone calcined clay cement (LC3), J. Clean. Prod. 412 (2023), 137394, https://doi.org/10.1016/j.jclepro.2023.137394.

[69] X. Jiang, R. Xiao, Y. Bai, B. Huang, Y. Ma, Influence of waste glass powder as a supplementary cementitious material (SCM) on physical and mechanical properties of cement paste under high temperatures, J. Clean. Prod. 340 (2022), 130778, https://doi.org/10.1016/j.jclepro.2022.130778.

[70] R. Xiao, B. Huang, H. Zhou, Y. Ma, X. Jiang, A state-of-the-art review of crushed urban waste glass used in OPC and AAMs (geopolymer): progress and challenges, Clean. Mater. 4 (2022), 100083, https://doi.org/10.1016/j.clema.2022.100083.

[71] W. Zhang, R. Zhang, C. Wu, A.T.C. Goh, S. Lacasse, Z. Liu, H. Liu, State-of-the-art review of soft computing applications in underground excavations, Geosci. Front. 11 (4) (2020) 1095–1106, https://doi.org/10.1016/j.gsf.2019.12.003.

[72] T. Wang, J. Wang, P. Wu, J. Wang, Q. He, X. Wang, Estimating the environmental costs and benefits of demolition waste using life cycle assessment and willingness-to-pay: a case study in Shenzhen, J. Clean. Prod. 172 (2018) 14–26, https://doi.org/10.1016/j.jclepro.2017.10.168.

[73] K. Chen, W. Lin, Q. Liu, B. Chen, V.W.Y. Tam, Micro-characterizations and geopolymerization mechanism of ternary cementless composite with reactive ultra-fine fly ash, red mud and recycled powder, Constr. Build. Mater. 343 (2022), 128091, https://doi.org/10.1016/j.conbuildmat.2022.128091.

[74] R. Kajaste, M. Hurme, Cement industry greenhouse gas emissions – management options and abatement cost, J. Clean. Prod. 112 (2016) 4041–4052, https://doi.org/10.1016/j.jclepro.2015.07.055.

[75] B.C. McLellan, R.P. Williams, J. Lay, A. van Riessen, G.D. Corder, Costs and carbon emissions for geopolymer pastes in comparison to ordinary portland cement, J. Clean. Prod. 19 (9) (2011) 1080–1090, https://doi.org/10.1016/j.jclepro.2011.02.010.

[76] Y. Zhang, M. Sun, J. Hong, X. Han, J. He, W. Shi, X. Li, Environmental footprint of aluminum production in China, J. Clean. Prod. 133 (2016) 1242–1251, https://doi.org/10.1016/j.jclepro.2016.04.137.

[77] Y. Zhang, X. Sun, X. Zhu, J. Xiao, Multi-criteria optimization of concrete mixes incorporating cenosphere waste and multi-minerals, J. Clean. Prod. 367 (2022), 133102, https://doi.org/10.1016/j.jclepro.2022.133102.